Draft version October 22, 2024
Typeset using LaTeX **twocolumn** style in AASTeX631

Inferring Asteroseismic Parameters from Short Observations Using Deep Learning: Application to TESS and K2 Red Giants

Nipun Ghanghas [1], Siddharth Dhanpal [1], Shravan Hanasoge [1,2], Praneeth Netrapalli [3] and Karthikeyan Shanmugam [3]

[1] *Department of Astronomy and Astrophysics, Tata Institute of Fundamental Research, Mumbai, 400005, India*
[2] *Center for Space Science, NYUAD Institute, New York University Abu Dhabi, PO Box 129188, Abu Dhabi, UAE*
[3] *Google Research India, Bengaluru, 560016, India*

ABSTRACT

Asteroseismology is the study of resonant oscillations of stars to infer their internal structure and dynamics. It is also a powerful tool for precisely determining stellar parameters such as mass, radius, surface gravity, and age. The ongoing TESS mission, with its nearly complete sky coverage, presents a unique opportunity to uniformly probe stellar populations across the Milky Way. TESS is estimated to have observed more than 300,000 oscillating red giants, most of which have one to two months of observations. Given the scale of this dataset, we need a fast, efficient, and robust way to analyse the data. In this work, our objective is to develop a machine learning based method to infer asteroseismic parameters from short-duration observations. Specifically, we focus on two global seismic parameters, the large frequency separation ($\Delta\nu$) and the frequency at maximum power ($\nu_{\rm max}$), from one-month-long TESS observations of red giants. Meanwhile, for K2 data, our focus extends to inferring the period spacings of dipolar gravity modes ($\Delta\Pi_1$), in addition to $\Delta\nu$ and $\nu_{\rm max}$. Our findings demonstrate that our machine learning algorithm can accurately infer $\Delta\nu$ and $\nu_{\rm max}$ for approximately 50% of samples created by taking one-month Kepler and K2 observations. For TESS one sector data however, we recover reliable $\Delta\nu$ for only about 10% of the stars. Additionally, we get reliable $\Delta\Pi_1$ inferences for about 90 young red-giants from K2. For these $\Delta\Pi_1$ inferences, we see a good match with the well known $\Delta\nu - \Delta\Pi_1$ observed in Kepler red-giants.

Keywords: Asteroseismology (73); Stellar oscillations (1617); Neural Networks (1933); Red giant stars (1372)

1. INTRODUCTION

Space-based missions such as CoRoT (Baglin et al. 2006), Kepler (Borucki et al. 2010), K2 (Howell et al. 2014) and TESS (Ricker et al. 2015) have provided vast datasets of high-precision photometric observations. These datasets are expected to increase significantly in size with upcoming missions such as PLATO (Rauer et al. 2024). Precise determination of fundamental stellar parameters such as mass, radius and age is made possible using asteroseismology. Red-giant asteroseismology is a powerful tool with which to probe populations throughout the Milky Way, enabling ensemble-scale galactic archaeology (Anders et al. 2017; Silva Aguirre et al. 2018; Sharma et al. 2019; Miglio et al. 2021).

Red giants also exhibit mixed modes, which behave as pressure modes in the envelop and gravity mode in the core. These mixed modes probe the stellar core and can put strong constraints on stellar evolution (Bedding et al. 2011; Mosser et al. 2011). These modes also allow us to infer period spacing of gravity modes which is directly related to core mass (Montalbán et al. 2013).

Kepler has observed ∼21,000 oscillating red giants (Hon et al. 2019; Dhanpal et al. 2022) in a 100 square-degree field in the northern hemisphere having four years of continuous observations. K2 observed ∼19,500 oscillating red giants (Zinn et al. 2022) in 18 Kepler sized fields along the ecliptic, each with three months

Corresponding author: Nipun Ghanghas
nipun@tifr.res.in

ghanghasnipun@gmail.com

of observation. TESS, with its vast coverage, is estimated to have observed more than 300,000 oscillating red giants (Mackereth et al. 2021) across the whole sky, with most of them observed for a duration of one to two months. The full sky coverage and an order of magnitude more oscillating red-giants provided by TESS makes it possible to study populations almost uniformly throughout the Milky Way.

Solar-like oscillations have been detected in subgiants and red giants observed by TESS using 1-2 sectors of short-cadence data. Hatt et al. (2023) analyzed both 2-minute and 20-second cadence data (Sectors 1 to 46) to identify 4,177 solar-like oscillators, reporting estimates of ν_{max} and $\Delta\nu$. More recently, Zhou et al. (2024) used 2-minute cadence data (Sectors 1 to 60) and expanded the number of detections to 8,651 stars, also providing estimates of stellar parameters such as radii, masses and surface gravity, in addition to global seismic parameters. For long cadence ($\sim$ 30 minutes) data, Silva Aguirre et al. (2020) used 1-2 sectors of TESS observations for bright red giants and found oscillations in all stars in the sample. Additionally, they obtained masses, radii and ages with uncertainties of approximately 3%, 5% and 20% respectively upon combining seismic inferences from TESS and parallaxes from Gaia DR2 (Gaia Collaboration et al. 2018). This is comparable to the precision achieved with full-length Kepler asteroseismic observations. Hon et al. (2022) analysed bright red giants from Henry Draper (HD) catalog located near TESS continuous viewing zones and having 1-2 years of observations. They obtained masses and radii with a precision of $\sim$ 8% and $\sim$ 3 %. Additionally, they also compared the asteroseismic radii obtained using scaling relations to with radii measured using interferometry for 16 giants and found a median fractional difference of only about $\sim$ 3%. Furthermore, Mackereth et al. (2021) used up to 13 sectors of data near the TESS continuous viewing zone in the southern hemisphere and recovered a median uncertainty of $\sim$8% in mass and $\sim$26% in age for a subset of the sample upon using Gaia luminosity as additional constraint in combination with asteroseismic inferences. They also show that these ages are precise enough to identify trends in galactic populations. Hon et al. (2021) used one sector TESS data and used ν_{max} inferences in combination with parallaxes, radial velocities and proper motions from Gaia EDR3 (Gaia Collaboration et al. 2021) to obtain a near all-sky Gaia-asteroseismology mass map, showing potential for all-sky galactic archaeology with TESS. Stello et al. (2022) analysed Kepler stars observed by TESS in one to two sectors and recovered ν_{max} and $\Delta\nu$ with uncertainties of $\sim$5% and $\sim$3% respectively. The short duration makes it challenging to infer detailed seismic parameters such as $\Delta\nu$ and they could reliably recovered $\Delta\nu$ in only about 20% (14% for one sector and 26% for two sectors) of the population.

Given the vast amount of data from the ongoing TESS mission, which will further increase with upcoming PLATO mission, we need a fast, efficient and robust way with which to infer seismic parameters from the photometric data.

Our aim in this work is to explore the possibility of (i) inferring $\Delta\nu$ and ν_{max} from one-month TESS observations and (ii) inferring $\Delta\nu$, ν_{max} and $\Delta\Pi_1$ from three-month K2 observations using methods based on machine learning.

For most cases, it is not possible to measure $\Delta\Pi_1$ from 1-2 sectors of TESS data owing to the short-observation duration and other systematics. However, three-month observations taken by K2 allowed us to retrieve $\Delta\Pi_1$ for about 90 young red giants.

2. DATA

2.1. *For TESS*

We use light-curves detrended using the co-trending basis vector (CBV) correction method implemented in the TASOC (TESS Asteroseismic Science Operations Center) pipeline developed by the coordinated activity TESS Data for Asteroseismology (T'DA) within the TESS Asteroseismic Science Consortium (TASC) (Handberg et al. 2021; Lund et al. 2021). We cross-matched the red giants identified by Hon et al. (2021) and used light-curves recorded at a cadence of 30 minutes for all the available stars. Instead of raw QLP data, which was used by Hon et al. (2021), we use the detrended data from TASOC pipeline because it is optimized for asteroseismology and preserves the stellar oscillation signal better that QLP, which is optimized for planet searches and removes stellar variability over long timescales while performing corrections. These detrended lightcurves from TASOC pipeline are useful for inferring $\Delta\nu$ from one-month TESS observations. We perform sigma clipping to reject flux values with more than 5-σ discrepancy. We also fill all gaps smaller than 1.5 hours in length using linear interpolation to minimize the impact of window function. Finally, we also reject stars with greater than 30% empty timestamps. We use the lightkurve package (Lightkurve Collaboration et al. 2018) to download light curves hosted at Mikulski Archive for Space Telescopes (MAST) and compute Lomb-Scargle periodograms (Lomb 1976; Scargle 1982; Press & Rybicki 1989). To make a uniform size sample, we use the same frequency range to calculate the power

spectral density (PSD) for all the stars, which is to be fed into the neural network for analysis. In total, we have 30,720 TESS red-giants for seismic analysis.

2.2. *K2 data*

We use detrended lightcurves form the `K2SFF` pipeline (Vanderburg & Johnson 2014) which performs corrections for trends related to spacecraft pointing and other systematics. We take the long cadence ($\sim$ 30 minutes) data for red-giant stars presented in K2 GAP DR3 (Zinn et al. 2022) and high-pass filter each lightcurve with a boxcar filter of width 4 days. Next, we perform sigma clipping to reject flux values with more than 5-σ discrepancy. Finally, we fill gaps shorter than 1.5 hours using linear interpolation. Again, we use the lightkurve package to download light-curves from MAST and compute Lomb-Scargle periodograms for all these stars with the same frequency range. In total, we have 11,264 K2 red-giants with $\Delta\nu$ in the range $4-19$ μHz, out of which 2,048 lie within $\Delta\nu$ range of $9-19$ μHz.

3. METHODS

We train deep neural networks to be able to infer seismic parameters directly from the PSD profiles, both for one-month TESS observations, hereafter referred to as the `TESS Model`, and three-month K2 observations, hereafter referred to as the `K2 Models` (`K2 Model-1 & 2`, collectively called `K2 Models`, see section 3.5 for details). Inputs to all the models are 1-D arrays of normalized power from the PSDs, without any background correction or feature extraction, and outputs are probability distributions for each parameter (see section 3.1). All the relevant features are learned by the neural networks on their own from the full PSD. Although the `TESS Model` and `K2 Models` differ in terms of kernel sizes and number of output parameters, the overall architecture is the same for all the models (see section 3.2).

3.1. *Converting regression problem to classification*

Identifying parameters corresponding to the PSD of a given star constitutes a regression problem. However, for each parameter, we divided the range of parameter values (which is continuous) into a fixed number of bins. We trained the model to classify the bin number for each parameter based on the given PSD, effectively converting the regression task into a classification problem. The model outputs an array of probabilities indicating the likelihood of each parameter belonging to a specific bin, for all target parameters. In machine learning, converting a regression task to a classification problem is a common approach, as it can often yield better performance (Stewart et al. 2022). This approach offers three key advantages: it significantly improves model accuracy, prevents unphysical predictions (such as negative values for $\Delta\nu$ or $\Delta\Pi_1$), which can occur in regression models, and provides a reliable estimate of uncertainty from the output probability distribution — something typically not achievable with regression models.

3.2. *Model architecture*

For our initial tests, we tried various NN architectures ranging from a vanilla CNN (Convolution Neural Network), CNN-LSTM (CNN in combination with Long-Short Term Memory), ResNet (Residual Network) to ViT (Vision Transformer). ResNet, which is a CNN with skip connections added between the layers, outperformed all other architectures that we tested for this particular task. Thus, we chose ResNet as our model and proceeded with fine tuning it further to improve accuracy. Fig 1 shows the architecture of `TESS Model` and `K2 Models`.

3.3. *Fine-tuning model hyperparameters*

We manually tuned the hyperparameters including kernel size, initial learning rate, number of ResNet blocks, dropout rate etc. `TESS Model` has a smaller kernel size of 21, compared to 51 for the `K2 Models`, to counter for the comparatively lower resolution of one month vs three months of data. Further, `TESS Model` has a higher dropout rate of 0.4, compared to 0.1 for the `K2 Models`, to avoid overfitting the small training dataset. The learning rate and batch size for all the models are the same, e.g., see section 3.5.

3.4. *Training data*

3.4.1. *For TESS*

To train the `TESS Model`, we use combined red-giants datasets from Kepler and K2 missions. For K2, we use data from K2 GAP DR3 (Zinn et al. 2022), which provided asteroseismic measurements of $\Delta\nu$ and $\nu_{\rm max}$ for 19,417 red giants. For Kepler, we use observations of 21,144 red giants, identified by (Dhanpal et al. 2022), who have also provided measurements of $\Delta\nu$ and $\nu_{\rm max}$ for these stars. To create training samples comparable in resolution to TESS 1-sector data, we divided each 4-year (in case of Kepler) and 3-month (in case of K2) light-curve into multiple, non-overlapping, 27-day segments. Due to the stochastic excitation of oscillations, each of these shorter-duration lightcurves has a unique noise profile. We note that this stochastic behavior may also lead to some of these shorter light-curves not showing solar-like oscillations.

Additionally, we also fill in gaps smaller than 1.5 hrs in duration using linear interpolation. Following this, we

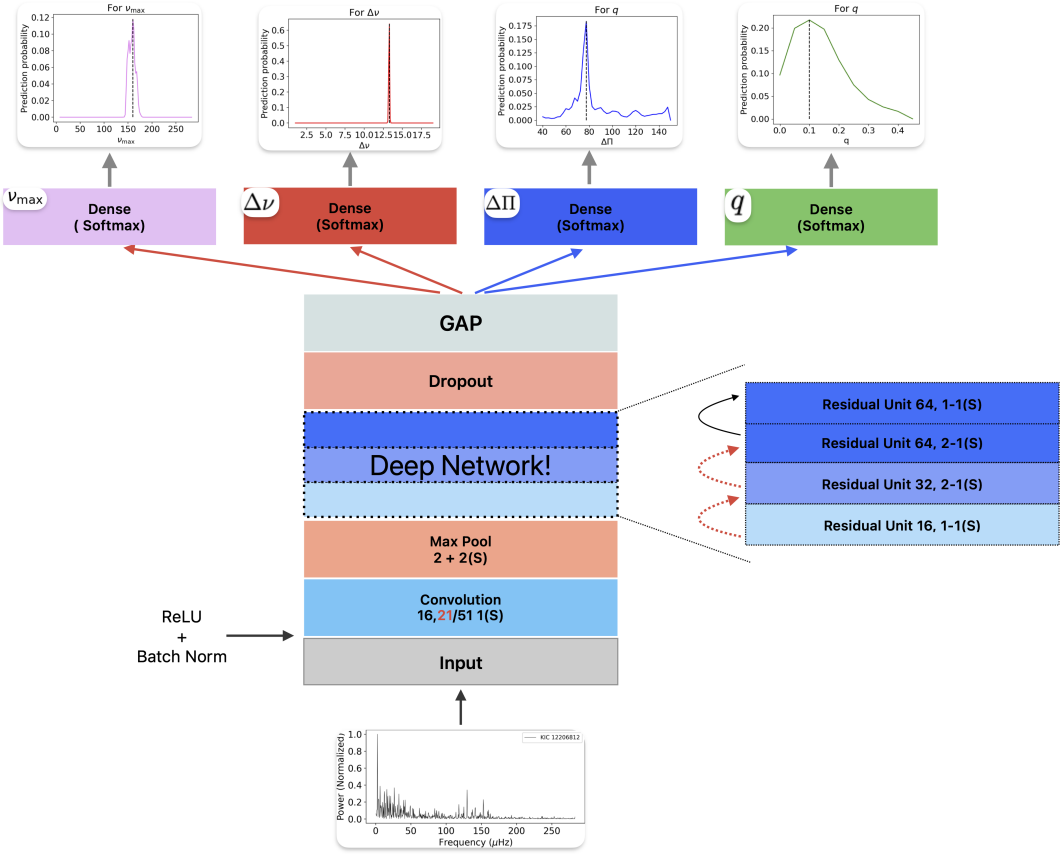

(a)

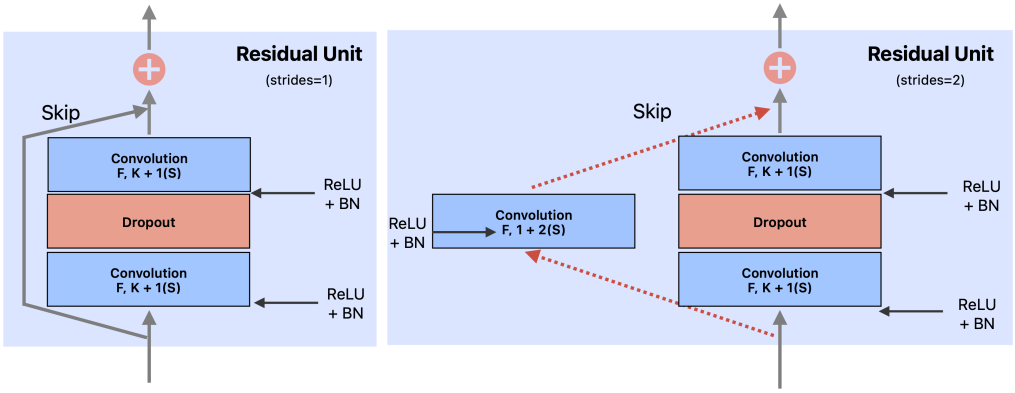

(b)

Figure 1: ResNet based model used for TESS and K2 **(a)** overall architecture and **(b)** the architecture of the residual units blocks, left for stride of 1 and right for stride of 2. **Note** : `TESS Model` has only two output parameters, ν_{max} and $\Delta\nu$.

discard all samples having more than 30% empty data points. In total, we have 822,274 samples, 768,267 from Kepler and 53,980 from K2. We use 70% of these data for training, 15% for validation and the remaining 15% as a test set.

The choice to use observations for training instead of synthetics is motivated by the links seen between granulation timescales, amplitudes and the positions of oscillations (Kallinger & Matthews 2010; Huber et al. 2011; Kjeldsen & Bedding 2011; Mathur et al. 2011; Chaplin et al. 2011; Yu et al. 2018). This was also emphasised by Hon et al. (2018) who used binned 2-D images of the PSD to identify presence of oscillations and estimate ν_{max}. These links could potentially help the neural network to better identify the position of the oscillations within the PSD. This becomes particularly important for datasets with short-duration observations, which have poor frequency resolution and low signal-to-noise ratios.

3.4.2. *For K2*

Unlike the `TSSS Model`, insufficient observational data are available to train the `K2 Models` - due to the limited number of $\Delta\Pi_1$ measurements for red giants. Hence, we generated synthetic dataset using the spectra simulator by Othman Benomar (Benomar 2023), which is based on asymptotic theory of stellar oscillations (Aerts et al. 2010; García & Ballot 2019). The theory and methodology used to generate synthetics is discussed briefly in appendix B.

We have built two separate datasets to train two distinct models, each containing approximately 10 million red-giants samples. Out of these datasets we use 82.5% as a training set, 15% as validation set and 2.5% ($\sim$ 320,000 samples) for testing. Both datasets have the same range of parameters except for $\Delta\nu$ and q. For the first dataset, $\Delta\nu$ lies in a range of $4-19$ μHz and q between $0.01-0.5$, while for the second dataset $\Delta\nu$ lies in the range $9-19$ μHz and q lies between $0.01-0.45$. Corresponding to the red-giant phase, $\Delta\Pi_1$ in both datasets spans the range 40-150 seconds. Table 2 shows the ranges of all the parameters used to create the synthetics and fig 11 shows an example of the synthetics we used for training, validation and testing the model.

To create these datasets, we uniformly sample the associated ranges for all the parameters except the inclination angle, which is sampled from an isotropic distribution $P(\iota) \propto sin\ \iota$. In particular, we have treated $\Delta\nu$, $\Delta\Pi_1$ and q as independent parameters, and while this may include samples which lack a corresponding theoretical model, we also do not inject a bias in training.

3.5. *Training*

We feed the normalized power from the PSD to the model and the corresponding bin number for all the output parameters ($\Delta\nu$ and ν_{max} for the `TESS Model` & $\Delta\nu$, ν_{max}, $\Delta\Pi_1$ and q for the `K2 Models`) to train the models. We use the ADAM optimizer in combination with cosine decay with restarts for the learning rate and train the models on 4 GPUs, with an initial learning rate of $1.5\text{x}10^{-4}/4$ and batch size of 64×4. Early stopping with a patience of 5 is used in training and we let the model training go on till this condition is met. Finally, the model with the lowest validation loss is saved and used for inferences.

3.5.1. *`TSSS Model`*

We trained the `TESS Model` on a one-month Kepler/K2-as-TESS dataset to predict $\nu_{\rm max}$ and $\Delta\nu$, with ranges of 8-283 μHz and 1-19 μHz, respectively. The bin sizes are set to 2 μHz for $\nu_{\rm max}$ and 0.1 μHz for $\Delta\nu$, corresponding to 139 and 181 bins, respectively. Both parameters are weighted equally in the loss function during model training to minimize validation loss.

3.5.2. *`K2 Models`*

For K2 data, we trained two separate models, each tailored to different parameter ranges, but with identical architectures. Both models output ν_{max}, $\Delta\nu$, $\Delta\Pi_1$, and q, differing only in the parameter ranges they cover:

(i) `K2 Model-1` operates over a $\Delta\nu$ range of $4-19$ μHz and a $\nu_{\rm max}$ range of $30-283$ μHz.

(ii) `K2 Model-2` operates over a $\Delta\nu$ range of $9-19$ μHz and a $\nu_{\rm max}$ range of $88-283$ μHz.

Each model consists of two sub-models: one optimized for inferring $\nu_{\rm max}$ and $\Delta\nu$ with weights (0.4, 0.4, 0.1, 0.1) assigned to $\nu_{\rm max}$, $\Delta\nu$, $\Delta\Pi_1$, and q respectively, and another optimized for inferring $\Delta\Pi_1$, with weights (0.1, 0.1, 0.7, 0.1). We use the $\nu_{\rm max}$ and $\Delta\nu$ predictions from the sub-model optimized for these parameters, and the $\Delta\Pi_1$ and q predictions from the sub-model optimized for $\Delta\Pi_1$.

The bin sizes for all models are 2 μHz for $\nu_{\rm max}$, 0.1 μHz for $\Delta\nu$, 2.5 seconds for $\Delta\Pi_1$, and 0.05 for q.

The necessity for different models arises from the challenge of inferring $\Delta\Pi_1$ from three-month observations. Dhanpal et al. (2023) demonstrated that it is possible to infer all four parameters from a single model using 4-year Kepler data. In particular, inferring $\Delta\Pi_1$ for evolved red giants and red-clump stars from just three months of observations is challenging due to the decreasing spacings between successive radial orders and the increasing granulation noise at lower frequencies. Additionally, as stars evolve, the mixed mode inertia increases, making

the modes less detectable (Grosjean et al. 2014), and the mixed mode density decreases with the onset of helium burning (Gehan et al. 2018), further adding to the difficulty of the measurement of period separation in these stars. While we initially attempted to infer $\Delta\Pi_1$ for stars across the $\Delta\nu$ range of $4-19$ μHz, useful inferences were obtained only for stars with $\Delta\nu$ above 9 μHz. This prompted the training of a separate model for the $\Delta\nu$ range of $9-19$ μHz, which proved more effective in inferring $\Delta\Pi_1$ within this range compared to the full-range model. Consequently, the $\Delta\Pi_1$ inferences presented here are derived exclusively from `K2 Model-2`, corresponding to young red giants.

4. RESULTS

4.1. *For TESS*

4.1.1. *Kepler/K2-as-TESS test set*

We first assess the performance of the `TESS Model` on sequences of one-month red-giant Kepler/K2 observations. Note that this dataset is not included in training or validation and is therefore unbiased. This test set is about 15% of the whole Kepler/K2-as-TESS red-giants dataset, comprising 112,640 samples. To filter out poor inferences, we select measurements with under-20% uncertainties in ν_{max} and under 5% for $\Delta\nu$. For all parameters, uncertainty is defined as the difference between the values at the 16th and 84th percentiles compared to the value at the 50th percentile from the output probability distribution. The total uncertainty, which is considered here, is taken as the absolute sum of these two differences. We have 96,066 ($\sim$ 85 %) of stars having ν_{max} uncertainty less than 20%, additional criterion of $\Delta\nu$ uncertainty less than 5% further reduces the sample to 59,095 stars ($\sim$ 50 % of the total). Of these 59,095 inferences, 99.8% have relative error in ν_{max} less than 20% and 96.1% have relative error in $\Delta\nu$ less than 5%. Fig 2a shows the comparison for `TSSS Model`-inferred ν_{max} from one-month chunks and the ν_{max} obtained from the full 4-year/3-month Kepler/K2 data. The plot is color coded with *confidence*, which is defined as the maximum value of the output probability distribution for the corresponding parameter for a given star. Fig 2b shows the same comparison for $\Delta\nu$. Overall, we see an excellent agreement for both ν_{max} and $\Delta\nu$ inferences for one-month and 4 years or 3-month observations. This is also reflected in the histogram of relative error in Fig 3. The increased spread in fractional residual for ν_{max} lower than 50 μHz (or $\Delta\nu$ lower than $\sim$ 5 μHz) is expected, as the frequency spacing between consecutive radial orders decreases and the convective noise becomes more prominent at these lower frequencies. The stratification observed in the fractional residual plot results from binning the parameter range.

4.1.2. *TESS red giants*

We applied the `TESS Model` to observations of 30,720 TESS red giants. Using the selection criterion of uncertainty less than 20% in ν_{max}, we identified 17,374 stars ($\sim$ 55 %). An additional criterion of uncertainty less than 5% in $\Delta\nu$ further reduced the sample to 3,002 stars ($\sim$ 10%). For these 3002 stars, we compare ν_{max} inferences from `TESS Model` with those obtained by Hon et al. (2021) in Fig 4a. The latter used a different machine learning technique to infer ν_{max} from one-sector raw-QLP data. We see a similar results as in the Kepler/K2-as-TESS test set, an excellent match for $\nu_{max} \geq 50\mu$Hz and increased spread in fractional residuals for stars with lower ν_{max}. We also observe a few cases of very fractional residual. Some differences might arise as a consequence of using data from different pipelines. Furthermore, Hon et al. (2021) use raw data from uncorrected lightcurves while we use detrended lightcurves which could lead to different values. Fig. 4b shows the histogram of relative errors for this sample, where we observe two peaks around fractional residuals of -0.06 and 0.06. These discrepancies are largely due to the assignment of ν_{max} to a one lower or higher bin. The small variations in ν_{max} estimates are likely caused by the identification of additional or missing peaks in the power excess envelope, resulting in slight over- or underestimation of $\nu_{\rm max}$ compared to Hon et al. (2021). Overall, ν_{max} for more than 98% of these 3002 stars show relative difference less than 20% and only 1% of the sample shows difference larger than 35% when compared with Hon et al. (2021). We found peaks related to systematics to be the main cause for large errors. Among the non-matching stars, we also find a small number of cases where predictions from our `TESS Model` are wrong, where it is misidentifying noise as ν_{max} while Hon et al. (2021) estimate ν_{max} correctly and vice-versa. Fig 5 shows the $\Delta\nu$ - ν_{max} plot for these TESS red-giants and it is seen that they follow the empirical relation established by Stello et al. (2009) for solar-like oscillators. ν_{max} comparison for the full sample of 17,374 stars is shown in appendix. Table 1 shows the results for ν_{max} and $\Delta\nu$ inferred from one-sector TESS data. We have flagged the stars where ν_{max} inferences differ by more than 35% from Hon et al. (2021) as having *mismatch* equal to 1. Parameter values for these mismatched stars could be inaccurate due to peaks arising from systematics in the PSD and we caution against using these inferences.

Note the significant difference in the yield of reliable in-

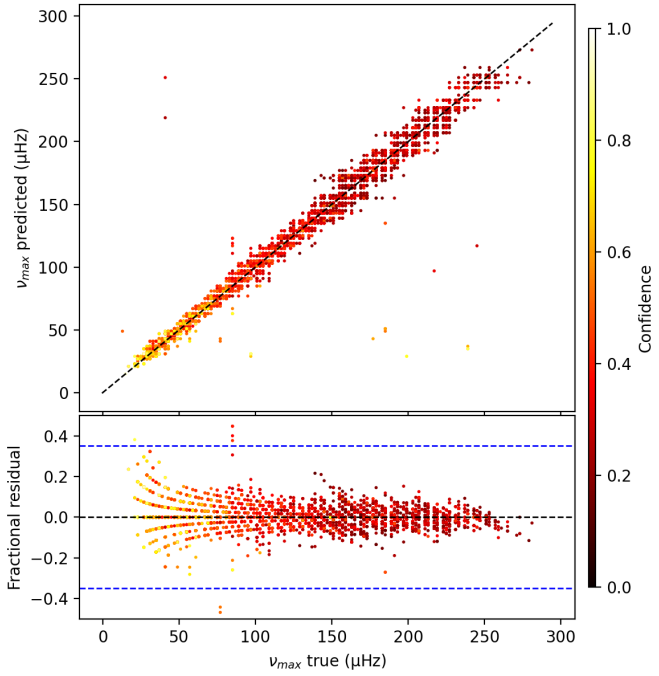

(a)

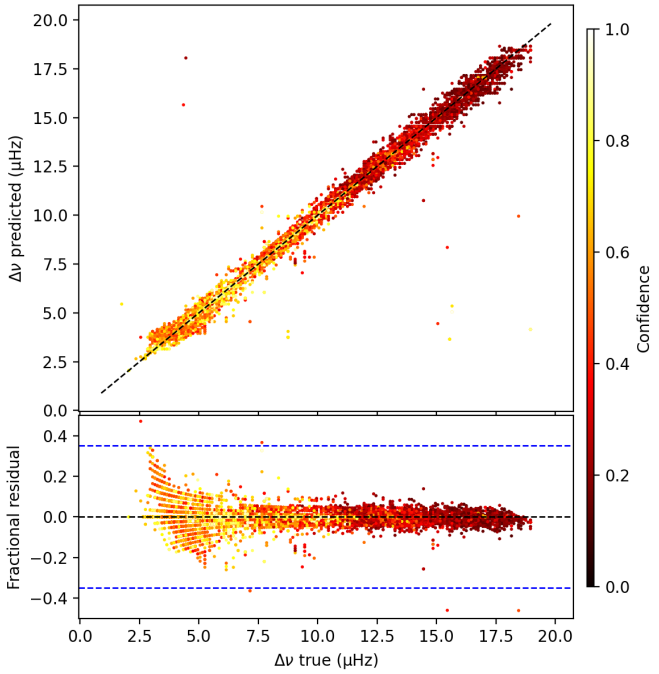

(b)

Figure 2: Panel (a) compares `TSSS Model`-inferred ν_{max} from one month chunks and ν_{max} obtained from the full 4 years/3-month Kepler/K2 data. *Confidence* refers to the maximum value in the output probability distribution for each star. The black dashed line in the top panel indicates the 1:1 line, while the two dashed blue lines in the bottom panel mark the ±0.35 fractional residuals, with the black dashed line denoting zero residual. The bottom panel's range is constrained from -0.5 to 0.5 for improved visibility. **(b)** is the same as (a) but for $\Delta\nu$.

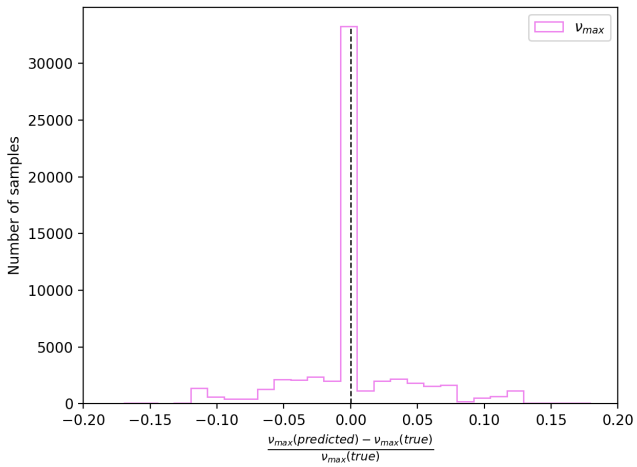

(a)

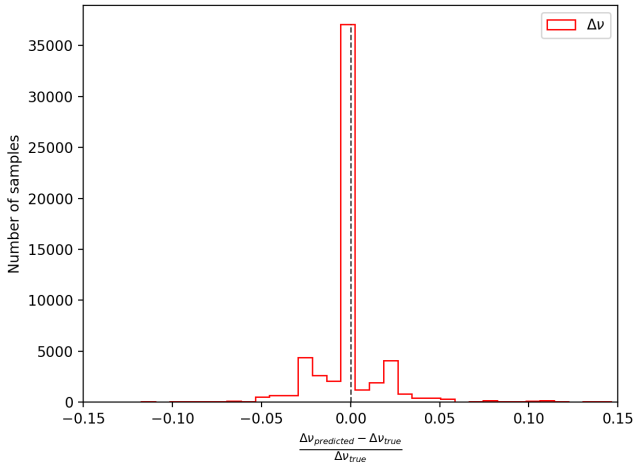

(b)

Figure 3: Histogram of fractional residuals/relative errors for the stars shown in Fig 2 **(a)** for ν_{max} and **(b)** for $\Delta\nu$

ferences between the Kepler/K2-as-TESS test set and TESS, particularly for $\Delta\nu$, 50 % vs 10 %. This lower yield for TESS red giants has been observed in previous studies as well, such as Stello et al. (2022), where $\Delta\nu$ could only be measured for 14 % of stars with one sector of data. One possible explanation for this discrepancy is the quality of photometric data from TESS, which is lower than that of Kepler, as TESS observations have lower photometric precision and are more susceptible to crowding effects (Sullivan et al. 2015). Furthermore, spacecraft systematics unique to TESS, which are absent in Kepler lightcurves and therefore not reflected in the training dataset could also increase the mismatch. Additionally, helium-core burning red

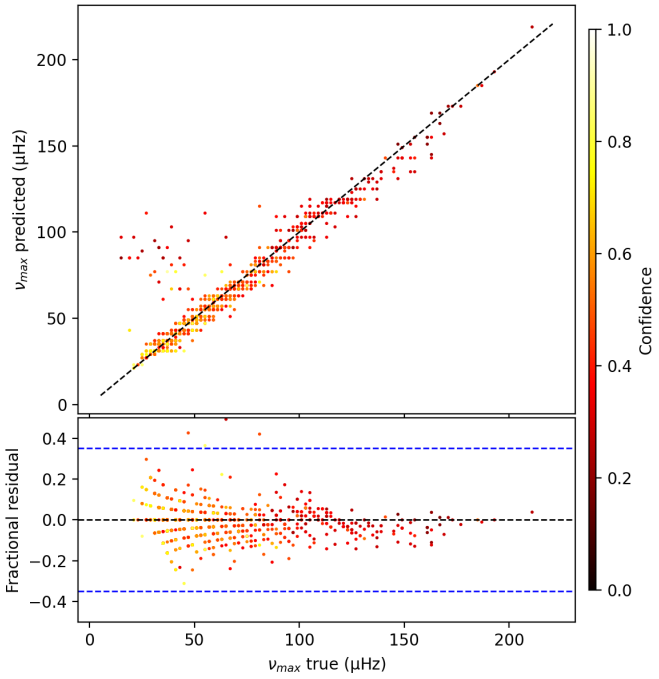

(a)

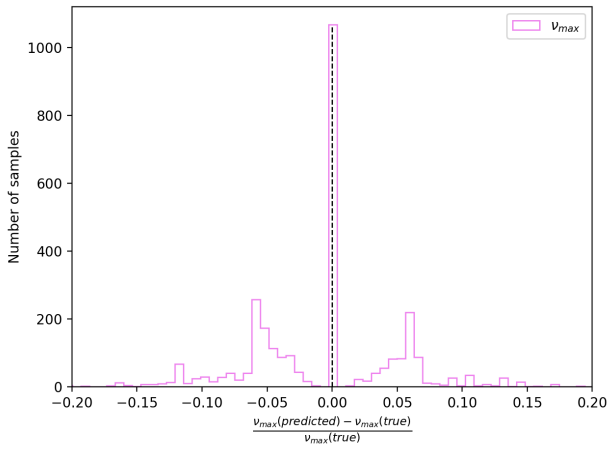

(b)

Figure 4: **(a)** Comparison between our ν_{max} inferences with those obtained by (Hon et al. 2021) for the 3002 stars with reliable $\Delta\nu$ inference. The lines and limits are the same as in Fig 2. **(b)** Histogram of fractional residual/relative difference for stars shown in (a).

clump (RC) stars, which dominate seismic detections from TESS (Hon et al. 2021; Stello et al. 2022), with ν_{max} in the 30-40 μHz range. Since extracting $\Delta\nu$ from RC stars is particularly challenging, this may also contribute to the lower yield.

4.2. *For K2*

To validate the performance of our `K2 Models`, we compare their inferences with published results in literature, shown in subsequent sections, as well as on synthetics, in appendix C.

4.2.1. *Comparison with K2 GAP DR3*

For the `K2 Model-1` we compare the predictions with with K2 GAP DR3 (Zinn et al. 2022). To filter for reliable inferences, we set an uncertainty threshold of less than 20% in ν_{max} and less than 10 % in $\Delta\nu$. Out of predictions for 11,264 stars from K2 GAP DR3 sample (with $\Delta\nu$ in the range of $4 - 19$ μHz), 9,009 stars satisfy this criterion. Fig 6a & Fig 6b shows the comparison between ν_{max} and $\Delta\nu$ inferences from the `K2 Model-1` with K2 GAP DR3 respectively. We see a similar trends as in the TESS results, an excellent match for $\nu_{max} \geq 50\mu$Hz and increased spread in fractional residuals for stars with lower ν_{max}. Overall, we observe a good match for both ν_{max} and $\Delta\nu$, with 97 % of stars having fractional difference in ν_{max} less than 20 % and 96 % stars having fractional difference in $\Delta\nu$ less than 10 %. Notably, we see a trend around $\Delta\nu \sim 12\mu$Hz and $\nu_{max} \sim 150\mu$Hz, this is due to the systematics related to the satellite thruster firings (see K2 data handbook for more details). Spurious peaks in PSD corresponding to harmonics of 47.19 μHz, caused due to thruster firings approximately every 6 hrs, have a mean around 150 μHz in these stars, leading to incorrect inferences.

4.2.2. *Kepler-as-K2*

To validate $\Delta\Pi_1$ inferences from the `K2 Model-2` on observations, we take three-month chunks of Kepler data for young red giants and compare the inferences from this dataset with stars in common from Vrard et al. (2016). However, as previously noted, the observational duration of 3 months makes it challenging to infer reliable $\Delta\Pi_1$ for most stars, as only a few dipole mixed modes are visible even in stars with good signal-to-noise ratio. We select only the stars with uncertainties less than 5% in $\Delta\Pi_1$ and q greater than 0.05 to ensure high-quality inferences. This additional constraint on q is applied because, for values below 0.05, both machine learning model predictions and MCMC fits for $\Delta\Pi_1$ tend to be unreliable, as demonstrated by Dhanpal et al. (2023) for Kepler red giants. Out of a total of 1,091 stars common with Vrard et al. (2016), this selection criterion leads to a final sample of 107 red giants. We obtain an excellent match for $\Delta\Pi_1$ for all but 4 of these 107 red-giants, see fig 7. Fig 8 shows the $\Delta\nu - \Delta\Pi_1$ plot for these stars, where most of these stars lie along the well known degenerate sequence. Notably there are 5 stars with $\Delta\Pi_1$ above 100 seconds - 4 of which do not match with Vrard et al. (2016). Fig 15 shows the output

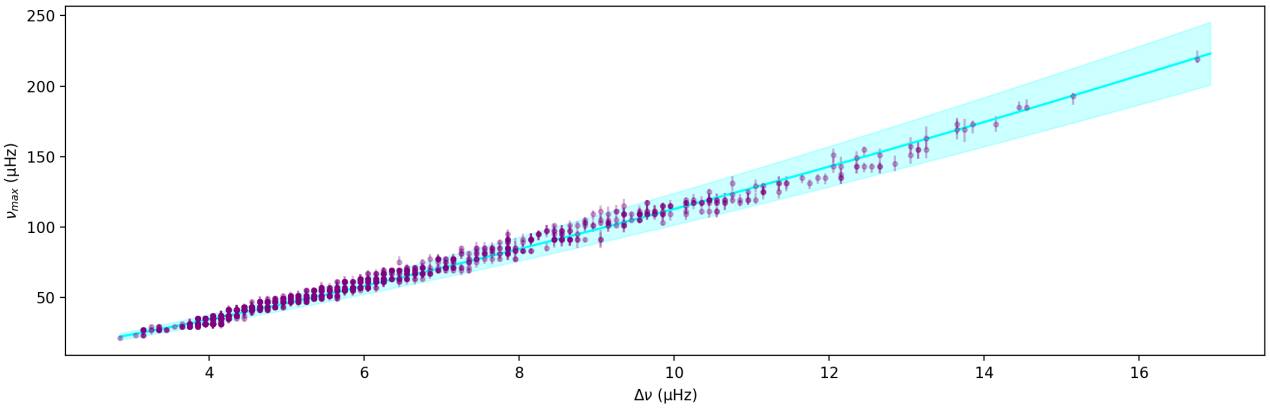

Figure 5: $\Delta\nu - \nu_{max}$ plot for `TESS Model` inferences from one-sector TESS red-giant data. The aqua line is the empirical relation given in Stello et al. (2009) and the shaded region represents 10% spread.

Table 1: Inferences for TESS red giants [a]

index	TIC	numax (μHz)	dnu (μHz)	err_numax (μHz)	err_dnu (μHz)	err_numax_left (μHz)	err_numax_right (μHz)	err_dnu_left (μHz)	err_dnu_right (μHz)	mismatch
1	316787599	29.0	4.15	2.92	0.14	1.16	1.76	0.06	0.08	0
2	154565606	29.0	3.95	2.19	0.15	0.94	1.25	0.06	0.08	0
3	121093011	15.0	5.75	2.41	0.07	1.37	1.04	0.04	0.04	1
4	154068647	35.0	4.05	3.68	0.2	1.94	1.73	0.09	0.11	0
5	462617902	31.0	3.95	1.71	0.14	0.86	0.86	0.05	0.08	0
...	...	...	...	...	...	...	...	...	...	...
17370	231733041	31.0	-	4.82	-	1.19	3.63	-	-	0
17371	146559499	35.0	-	3.09	-	1.28	1.82	-	-	0
17372	175316255	41.0	-	5.09	-	3.74	1.35	-	-	0
17373	103743056	31.0	-	2.51	-	1.46	1.05	-	-	0
17374	143211335	37.0	-	6.46	-	2.49	3.96	-	-	0

[a] Note: The full table is provided as supplementary material.

probability distribution for one of these five star where our prediction of $\Delta\Pi_1$ matched with that of Vrard et al. (2016). Upon examining the output $\Delta\Pi_1$ probability distribution for these four anomalous stars, we find multiple peaks in three and very small peaks in another (see figure 16 in appendix). Interestingly, our model also predicts - albeit with low probability - the value reported by Vrard et al. (2016) in these four stars. This small peak falls on the well known $\Delta\nu - \Delta\Pi_1$ red-giant degenerate sequence. Detailed investigation of this is beyond the scope of our current work.

4.2.3. *Results on K2 red-giants*

We apply `K2 Model-2` on 2,048 K2 red giants with $\Delta\nu > 9$ μHz from the K2 GAP DR3 catalogue. Keeping the same selection criterion of uncertainty in $\Delta\Pi_1$ of less than 5% and q greater than 0.05 we have a total of 97 confident inferences. Fig 9 shows the $\Delta\nu - \Delta\Pi_1$ plot for these stars plotted over the Kepler red giants from Vrard et al. (2016). We find all but 6 of the red giants having a $\Delta\Pi_1 < 100$ μHz and aligning with the degenerate sequence. Four of the five outliers show multiple peaks in the output $\Delta\Pi_1$ probability distribution like Kepler-as-TESS outliers and the other two are close to the upper edge of the parameter range. Table 3 shows the parameters values of these 97 red-giants. We have flagged inferences with $\Delta\Pi_1 > 100$ seconds in the catalogue as anomalous, which require further study.

5. SUMMARY AND CONCLUSIONS

We have developed deep learning based techniques to infer seismic parameters from short-duration observations. The model takes in normalized PSD as input and provides probability distribution for each parameter as output. All the relevant features are learned by the model on it's own, eliminating the need for background fitting or mode identification. Specifically, we infer ν_{max} & $\Delta\nu$ from one-sector TESS data and $\Delta\Pi_1$ from three-month K2 observations. The `TESS Model` is trained on PSDs corresponding to one-month chunks

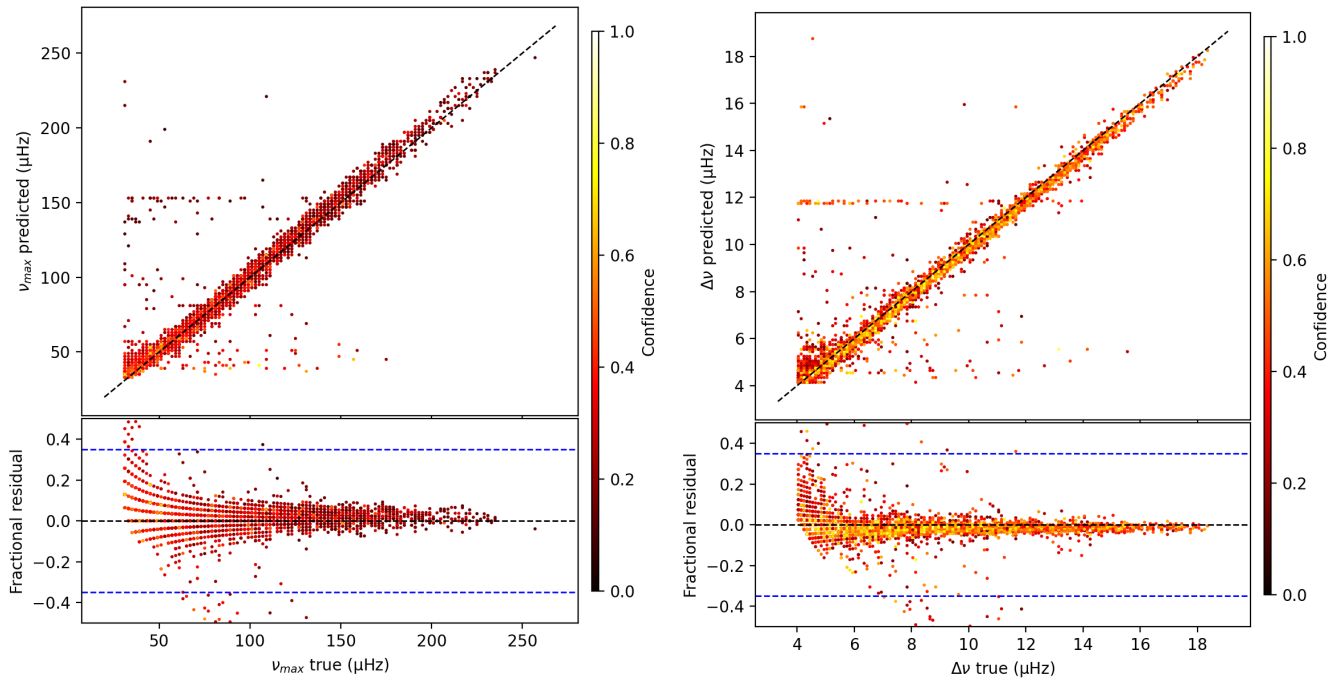

Figure 6: Comparison of `K2 Model-1` inferences from K2 observations with K2 GAP DR3 (Zinn et al. 2022) (a) for ν_{max} and (b) for $\Delta\nu$. The lines and limits are the same as in Fig 2.

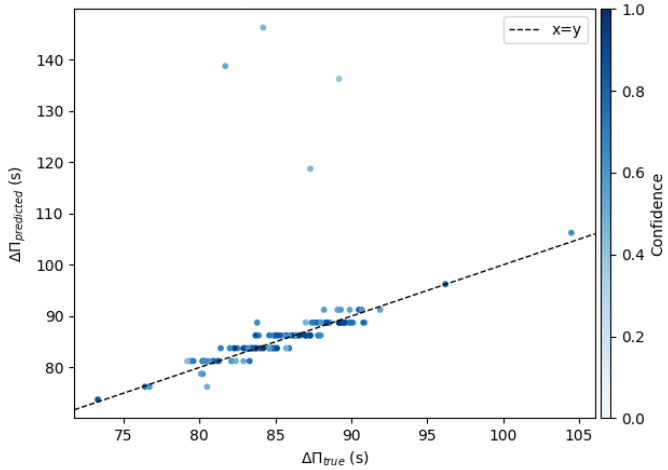

Figure 7: Comparison of $\Delta\Pi_1$ inferences for 107 stars by `K2 Model-2` from 3-month Kepler-as-K2 data with inferences from the 4-year dataset by Vrard et al. (2016).

from Kepler and K2 red-giant lightcurves. To train `K2 Models`, we created synthetic datasets. We also demonstrated the performance of `K2 Model-2` , which is used for $\Delta\Pi_1$ inferences, on a set of unseen synthetics. Our main findings are summarized as follow:

- We validated the `TESS Model` performance on one-month chunks from Kepler/K2 and found a good match with the true values obtained from 4 years/3 months of Kepler/K2 observations for reliable inferences. We have 96,066 stars ($\sim$ 85 %) out of a total set of 112,640 having ν_{max} uncertainty less than 20%, additional criterion of $\Delta\nu$ uncertainty less than 5% further reduces the sample to 59,095 stars ($\sim$ 50 % of the total). Of these 52,978 inferences, 99.8% have relative error in ν_{max} less than 20% and 96.1% have relative error in $\Delta\nu$ less than 5%.

- We applied the `TESS Model` to 30,720 TESS red giants, obtaining reliable ν_{max} for 17,374 stars (55 %) using the same uncertainty threshold. Additional criterion on $\Delta\nu$ reduced the sample to 3,002 stars (10 % of the total). Of these 3,002, more than 98.6 % had a relative difference in ν_{max} of less than 20 % when compared with Hon et al. (2021), while 90 % of the full sample of 17,374 stars fell within the same threshold. Additionally, all stars in this subset followed the $\Delta\nu$–$\nu_{\rm max}$ relation for solar-like oscillators.

- We compared $\nu_{\rm max}$ and $\Delta\nu$ inference from K2 Model with K2 DR3 catalogue for 9,009 stars having ν_{max} and $\Delta\nu$ uncertainties less than 20 % and 10 % respectively out of a set of 11,264 stars. The results show a a good overall match, with 97 % of stars having fractional difference in ν_{max} less than

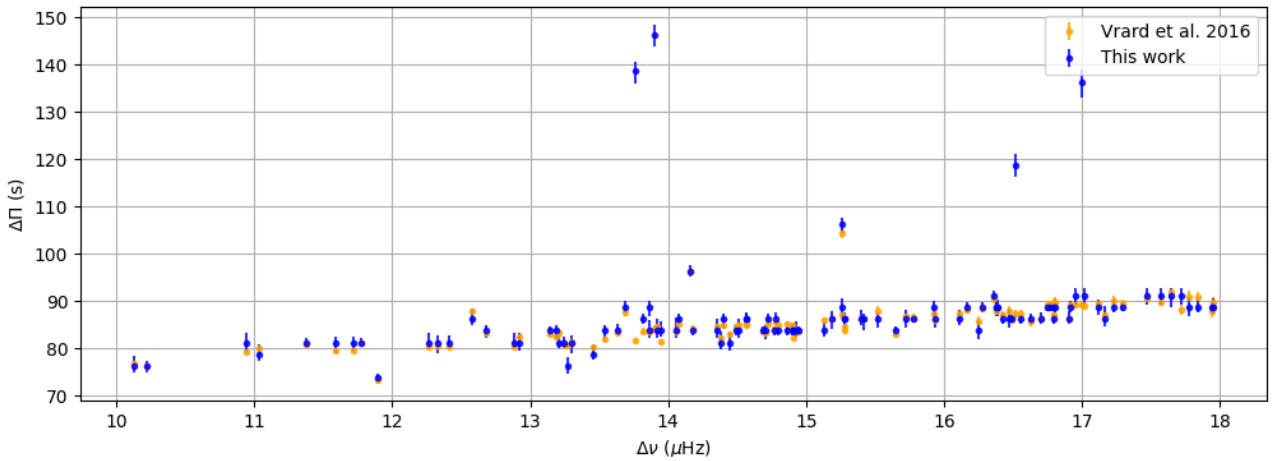

Figure 8: $\Delta\nu - \Delta\Pi_1$ plot for 107 common red-giants from 3-month Kepler-as-K2 data (in blue), plotted over inferences from the 4-year dataset by Vrard et al. (2016) (in orange).

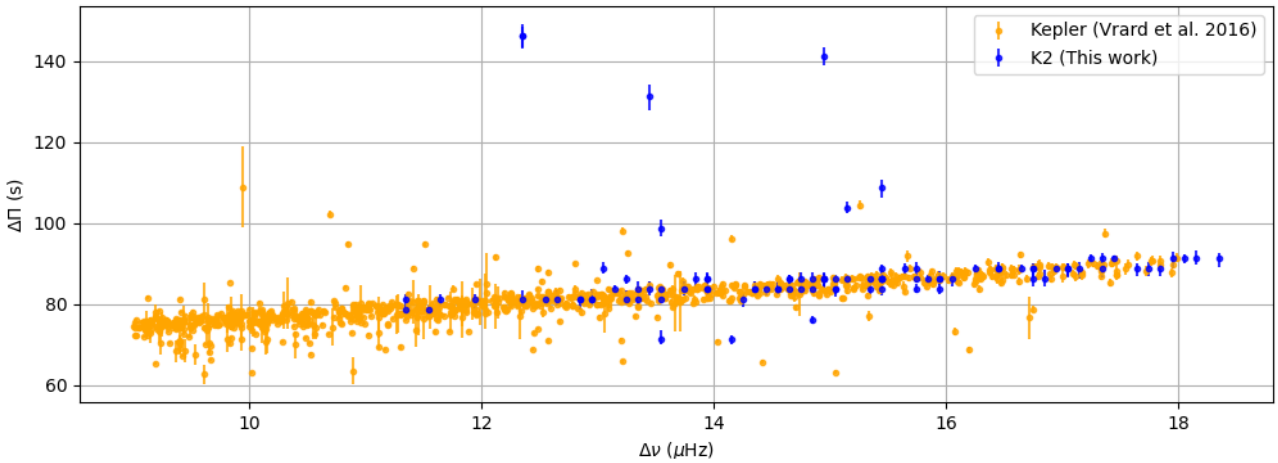

Figure 9: $\Delta\nu - \Delta\Pi_1$ plot for K2 red-giants (in blue) plotted over Kepler red giants (in orange) from Vrard et al. (2016).

20 % and 96 % stars having fractional difference in $\Delta\nu$ less than 10 %.

- We validated the performance of `K2 Model-2`, the model used for $\Delta\Pi_1$ inferences, on a set of synthetics of young red-giants with $\Delta\nu$ range $9 - 19$ μHz. For all selected inferences, we saw an excellent match for the three parameters ν_{max}, $\Delta\nu$ and $\Delta\Pi_1$.

- We also demonstrated the reliability of $\Delta\Pi_1$ inferences by applying the model on three-month Kepler data of young red giants and comparing it with the values reported by Vrard et al. (2016) from 4-year Kepler observations. We obtained reliable inferences for 107 out of a total of 1,091 common stars, of which we have good matches in $\Delta\Pi_1$ for 103 stars. 4 non-matching stars do not follow the typical $\Delta\nu - \Delta\Pi_1$ degenerate-sequence relation and may be easily identified as outliers. Interestingly, the probability distributions for all the four stars also show a small peak at around the values reported by Vrard et al. (2016).

- We report $\Delta\Pi_1$ inferences for 97 K2 red-giants which are found to be reliable out of a set of 2,048 stars. All of these except 6 have $\Delta\Pi_1$ below 100 s and follow the well-known $\Delta\nu - \Delta\Pi_1$ relation. These 6 stars are flagged as anomalous in the final catalogue.

6. FUTURE GOALS

We plan to extend this analysis to the full sample of more than 300,000 TESS red-giants which have now been observed in multiple sectors. The addition of 1-2 sector of observations for each star would further improve the frequency resolution and the SNR of the sig-

nal, which should lead to a higher yield for reliable ν_{max} as well as $\Delta\nu$ measurements. Furthermore, we plan to try and infer $\Delta\Pi_1$ for all the TESS red giants having more than six months of data. For this analysis, we plan on using detrended TESS lightcurves from which systematical errors have been removed and which will be made available in the near future (private communication, Rafael Garcia).

7. ACKNOWLEDGEMENTS

NG acknowledge support from the Department of Atomic Energy, Government of India, under Project Identification No. RTI 4002 and Google Research India for providing credits to be used in computational resources. NG would like to thank Shatanik Bhattacharya (TIFR) for all the helpful discussions. This paper includes data collected by the Kepler, K2 and TESS missions and obtained from the MAST data archive at the Space Telescope Science Institute (STScI). Funding for the Kepler, K2 and TESS missions is provided by the NASA Science Mission Directorate. STScI is operated by the Association of Universities for Research in Astronomy, Inc., under NASA contract NAS 5-26555. This research made use of Lightkurve, a Python package for Kepler, K2 and TESS data analysis (Lightkurve Collaboration et al. 2018). This research was supported in part by a generous donation (from the Murty Trust) aimed at enabling advances in astrophysics through the use of machine learning. Murty Trust, an initiative of the Murty Foundation, is a not-for-profit organisation dedicated to the preservation and celebration of culture, science, and knowledge systems born out of India. The Murty Trust is headed by Mrs. Sudha Murty and Mr. Rohan Murty. *Software*: NumPy (Harris et al. 2020), Lightkurve (Lightkurve Collaboration et al. 2018), TensorFlow Abadi et al. (2015), Pandas (Reback et al. 2022).

APPENDIX

A. COMPARISON FOR ALL RELIABLE INFERENCES FROM TESS SET

Fig 10a shows the ν_{max} inferences comparison with (Hon et al. 2021) for 17,374 stars out of 30,720 stars having uncertainty in ν_{max} less than 20 %. Note that unlike other plot in this work, this is a simple scatter plot where darker regions corresponds to more number of samples. Fig 10b shows the histogram of relative difference for these stars. As in Fig 4b, we observe two noticeable peaks around the fractional residuals of -0.06 and 0.06. Overall, 87.4% of stars have relative difference in ν_{max} less than 20 % and only 10% of stars have relative difference greater than 35%. The large differences observed for this small subset of stars can primarily be attributed to the spurious peaks present in the power spectral density profiles of certain stars, leading to inaccurate estimates. Additionally, some of these discrepancies can be explained by the use of different lightcurve sets in the two analyses, which were processed through different pipelines.

B. CREATING SYNTHETICS

The detailed formulation for generating synthetics may be found in Benomar (2023) and Dhanpal et al. (2022). Here, we briefly summarise the overall methodology applied to generate the synthetics.

B.1. *Mode frequencies*

The asymptotic theory of oscillations of p modes in red giants may be expressed as (Mosser et al. 2012),

$$\frac{\nu_{n_p,l}}{\Delta\nu} = n_p + \frac{l}{2} + \epsilon_p(\Delta\nu) - d_{0l}(\Delta\nu) + \frac{\alpha_l}{2}\left[n_p - \frac{\nu_{max}}{\Delta\nu}\right]^2, \tag{B1}$$

where $\Delta\nu$ is large separation, ν_{max} is the frequency at maximum power, n_p is the p-mode radial order, ℓ is the angular degree, ϵ_p is the phase offset, $d_{0\ell}$ is the small frequency separation and α_ℓ, the degree-dependent gradient $\alpha_\ell = (d\ \log\Delta\nu/dn)_\ell$.

Mixed-mode frequencies for red giants are given by an implicit equation (Mosser et al. 2015),

$$\tan\pi\frac{\nu-\nu_p}{\Delta\nu} = q\ \tan\frac{\pi}{\Delta\Pi_1}\left(\frac{1}{\nu} - \frac{1}{\nu_g}\right), \tag{B2}$$

where ν_g is the asymptotic frequency of pure g modes. For dipole modes $\nu_g = 1/(-n_g + \epsilon_g)\ \Delta\Pi_1$, where n_g is the radial order and ϵ_g is the offset parameter for g modes.

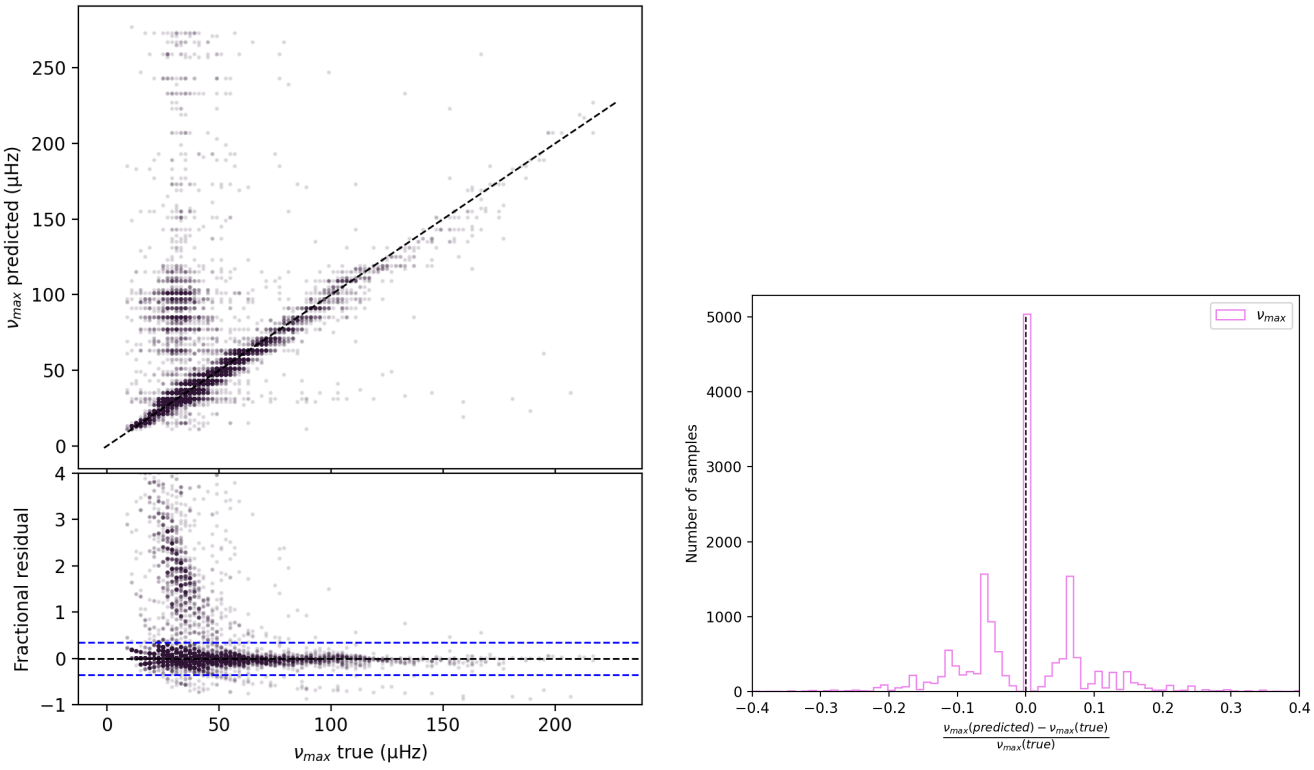

(a) (b)

Figure 10: **(a)** Comparison between our ν_{max} inferences with those obtained by (Hon et al. 2021). The bottom panel's range is constrained from -1 to 4 for improved visibility. The lines are the same as in Fig 2. **(b)** Histogram of fractional residual/relative difference for stars shown in (a).

We solve equation B1 to determine frequencies of ℓ=0, 2 and 3 modes, which are treated as pure pressure modes in our synthetics. To determine the frequencies of dipole mixed modes, we take solutions of the implicit equation B2 in a range of 1.2 times $\Delta\nu$ for each pure ℓ=1 p mode.

B.2. *Rotational splittings*

Rotation breaks the spherical symmetry of the star and lifts the degeneracy in m, splitting each mode of degree ℓ into $2\ell+1$ azimuthal components. The frequency of each of these components is given by $\nu_{n,\ell,m} = \nu_{n,\ell} + \delta\nu_{n,\ell}$, where $\delta\nu_{n,\ell}$ is the rotational splitting. For p-modes in solar-like stars, the dependence of rotational splitting on (n, ℓ) is weak within the observed frequency range (Lund et al. 2014). Rotational splittings for p-modes may be approximated as,

$$\nu_{n,\ell,m} = \nu_{n,\ell} - m\ \delta\nu_{n,\ell} \quad , \tag{B3}$$

where $\delta\nu_{n,\ell} = \Omega/2\pi$ is a function only of average internal rotation rate Ω. Furthermore, owing to the large envelopes in red giants and the high sensitivity of p-modes rotational kernels to the outer layers of the star, it is common to approximate average rotation as $\Omega \simeq \Omega_{env}$ and hence $\delta\nu_{n,l} \simeq \Omega_{env}/2\pi$ (Goupil et al. 2013).

Mixed modes on the other hand are influenced by both the core and the envelope. For $\ell = 1$ mixed modes in red giants and early subgiants, a two-zone model of rotation can be used to estimate the rotational splittings as shown by Goupil et al. (2013). Moreover, they also demonstrate that the contribution from core and envelope to the rotational splitting depends upon the ratio $\zeta(\nu)$ of kinetic energy of the modes in g-cavity and the total kinetic energy of modes as,

$$\delta\nu_{rot} = -\frac{1}{2}\frac{\Omega_{core}}{2\pi}\zeta(\nu) + \frac{\Omega_{env}}{2\pi}(1-\zeta(\nu)). \tag{B4}$$

Additionally, Deheuvels et al. (2015) showed that $\zeta(\nu)$ is well approximated by,

$$\zeta(\nu) = \left[1 + \frac{1}{q}\frac{\nu^2 \Delta\Pi_1}{\Delta\nu}\frac{cos^2\pi\frac{1}{\Delta\Pi_1}\left(\frac{1}{\nu}-\frac{1}{\nu_g}\right)}{cos^2\pi\frac{\nu-\nu_p}{\Delta\nu}}\right]^{-1}. \tag{B5}$$

B.3. *Heights and Widths of modes*

Each oscillation mode is modeled as a Lorentzian centered around $\nu(n,\ell,m)$ with height $H(n,\ell,m)$ and linewidth $\Gamma(n,\ell,m)$. To obtain realistic mode heights and widths for $\ell = 0, 2$ and 3 p modes, we use mode amplitudes and linewidths from templates of red giants and sub-giants observed by Kepler, rescaling them depending on ν_{max} and $\Delta\nu$, following a technique similar to Kamiaka et al. (2018). See Dhanpal et al. (2022) for an example of this technique. Mixed-mode amplitudes and linewidths of dipole modes are obtained by scaling radial modes using ratios of the kinetic energies of modes in g-mode cavity to the total kinetic energies of modes, $\zeta(\nu)$,

$$A_1^2(\nu) = A_0^2(1-\zeta(\nu)); \quad \Gamma_1(\nu) = \Gamma_0(1-\zeta(\nu)). \tag{B6}$$

The heights $H(n,\ell,m)$ of modes are determined as

$$H(n,\ell,m) = r_{\ell,m}(\iota)V(\ell)A_n, \tag{B7}$$

where $V(\ell)$ is the mode visibility, A_n is the amplitude of the mode with radial order n and $r_{\ell,m}(\iota)$ is the relative amplitude of the mode which depends on the inclination angle ι, determined according to

$$r^2_{\ell,m}(\iota) = \frac{(\ell-|m|)!}{(\ell+|m|)!}[P_\ell^{|m|}(cos\iota)]^2, \tag{B8}$$

where $P_\ell^{|m|}$ is the associated Legendre polynomial.

B.4. *Noise Model*

The noise model comprises two components, a Harvey-like profile generated by surface granulation and white noise which is frequency independent. At low frequencies, the granulation component dominates and at high frequencies, white noise is the primary contributor. We do not consider additional facular signatures in our synthetics.
The noise model is given by

$$B(\nu) = \frac{H_g}{1+(\tau\nu)^{\mathrm{p}}} + N_0, \tag{B9}$$

where the first term is the Harvey-like component which depends on the characteristic granulation amplitude H_g, the granulation timescale τ, and power-law exponent p. The second term, N_0, represents white noise.
Furthermore, granulation amplitude and timescale have been observed to vary with ν_{max} (Kallinger & Matthews 2010; Mathur et al. 2011; Chaplin et al. 2011). Hence, the granulation amplitude and timescale are modeled as,

$$H_g = A_g\nu_{max}^{B_g} \; + \; C_g \; , \quad \tau = A_\tau\nu_{max}^{B_\tau} \; + \; C_\tau, \tag{B10}$$

where (A_g, B_g, C_g) and (A_τ, B_τ, C_τ) are free parameters which control the granulation amplitude and timescale respectively.

B.5. *Power Spectrum Model*

The power spectrum model comprises two parts, the oscillation signal S and noise profile B. The oscillation signal is a sum of Lorentzians centered around the respective mode frequencies, given by,

$$S(\nu) = \sum_n \sum_{\ell=0}^{3} \sum_{m=-\ell}^{\ell} \frac{H_{n\ell m}}{1+4\left(\frac{\nu-\nu_{n\ell m}}{\Gamma_{n\ell m}}\right)^2}. \tag{B11}$$

Mode frequencies $\nu_{n\ell m}$, height $H_{n\ell m}$ and width $\Gamma_{n\ell m}$ of Lorentzian peaks are determined as explained previously. For a given set of parameters, the the power spectrum model is calculated by adding signal and noise profile part as,

$$M(\nu) = S(\nu) \; + \; B(\nu). \tag{B12}$$

We then multiply a random realisation of chi-squared noise with two degrees of freedom to the resulting model to obtain the synthetic PSD profile.

Table 2: Ranges of seismic parameters used to create the synthetics dataset

Parameter	Dataset 1	Dataset 2	Distribution
$\Delta\nu$ (μHz)	4–19	9–19	Uniform
$\Delta\Pi_1$ (s)	40–150	40–150	Uniform
q	0–0.5	0–0.45	Uniform
ϵ_p	0–1	−1–0	Uniform
ϵ_g	0–1	−1–0	Uniform
α_ℓ	0.0–0.008	0.0–0.008	Uniform
Core rotation (μHz)	0.005–2.8	0.005–2.8	Uniform
Envelope rotation (μHz)	0.005–0.4	0.005–0.4	Uniform
Inclination ι (deg)	0–90	0–90	Isotropic
A_g	0.8–1.2	0.8–1.2	Uniform
B_g	−2.2 to −1.8	−2.2 to −1.8	Uniform
C_g	0–1.0	0–1.0	Uniform
A_τ	0.8–1.2	0.8–1.2	Uniform
B_τ	−1.2 to −0.9	−1.2 to −0.9	Uniform
C_τ	0–1.0	0–1.0	Uniform
p	1.8–2.4	1.8–2.4	Uniform
N_0	1–2000	1–2000	Uniform
Noise Realisations	1–3	1–3	Uniform
Frequency range for ML training (μHz)	3.02–277.77	3.02–277.77	2088 bins
Observation time (days)	88.0	88.0	Fixed value
SNR	10–23	10–23	Uniform

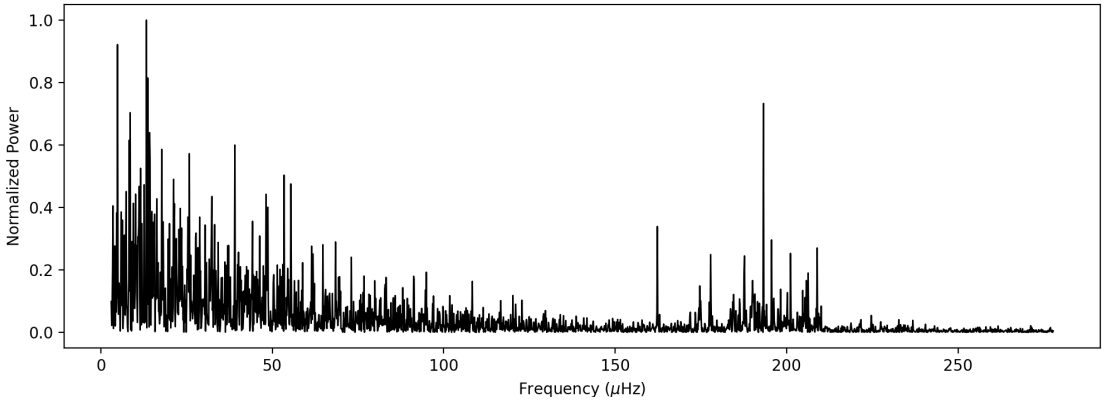

Figure 11: Example of K2-like resolution in a synthetic PSD with $\nu_{max} = 197.81\mu$ Hz, $\Delta\nu = 15.62\mu$ Hz, $\Delta\Pi_1 = 58.56$ seconds and $q = 0.42$.

C. RESULTS ON SYNTHETICS

We created a set of synthetics to test `K2 Model-2` performance on completely unbiased samples. We use the same selection criterion of $\Delta\Pi_1$ uncertainty less than 5% and q greater than 0.05 to maintain consistency and enable comparisons between model inferences and the ground-truth values used to create the synthetics. This selection criterion allows in 18,835 stars out of the full test set of 79,104 stars. Fig 12a, 12b and 14a shows the comparison for predictions vs true values for ν_{max}, $\Delta\nu$ and $\Delta\Pi_1$ for these stars respectively. We see a near perfect match, with ν_{max} error less than 10 %, $\Delta\nu$ error less than 2.5 % and $\Delta\Pi_1$ error less than 5% for all of the stars; see Figs. 13a, 13b and 14b.

Machine-learning models are able to distinguish the noisy part of the PSD from signal after training. We tested this capability by applying models trained on PSDs without background correction to datasets where convection noise had been estimated and divided out. The prediction accuracies for all parameters remained nearly identical to those obtained using the original data containing convection noise. This is expected for synthetics as we chose the

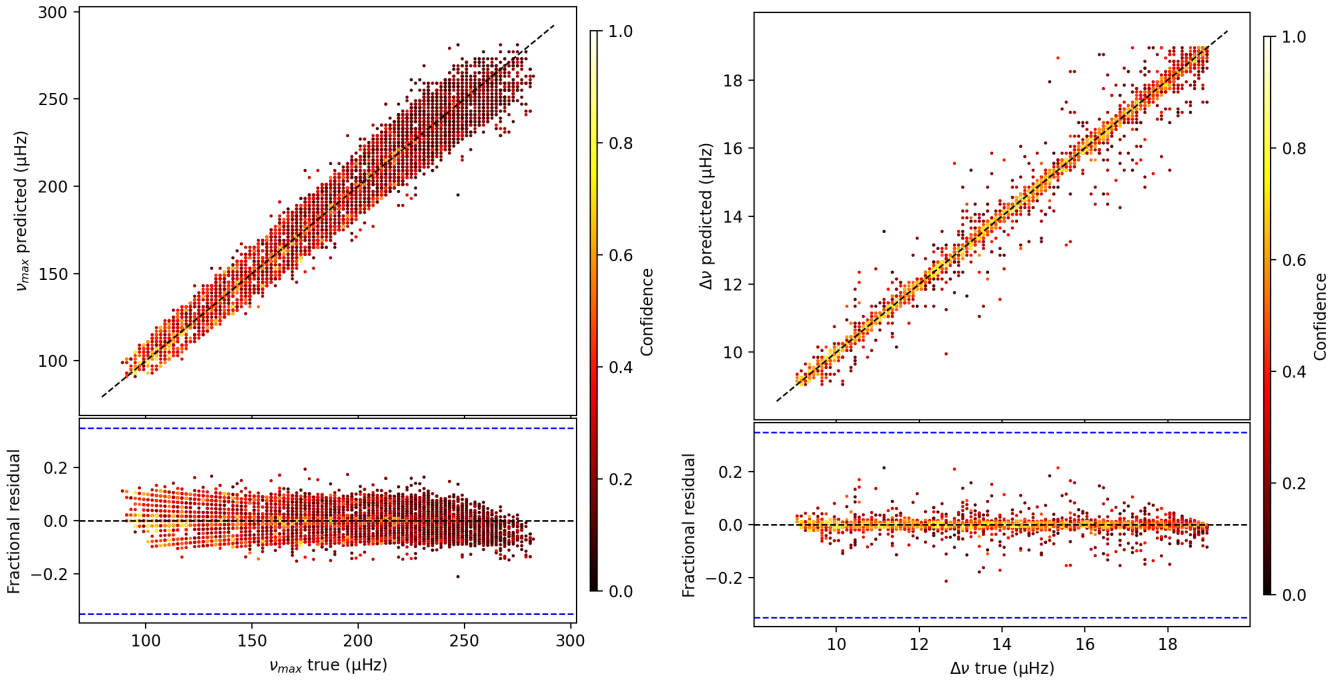

(a) (b)

Figure 12: Comparison of `K2 Model-2` inferences from the test set of synthetics with true values for ν_{max} (panel a) and $\Delta\nu$ (panel b). The lines and limits are the same as in Fig 2.

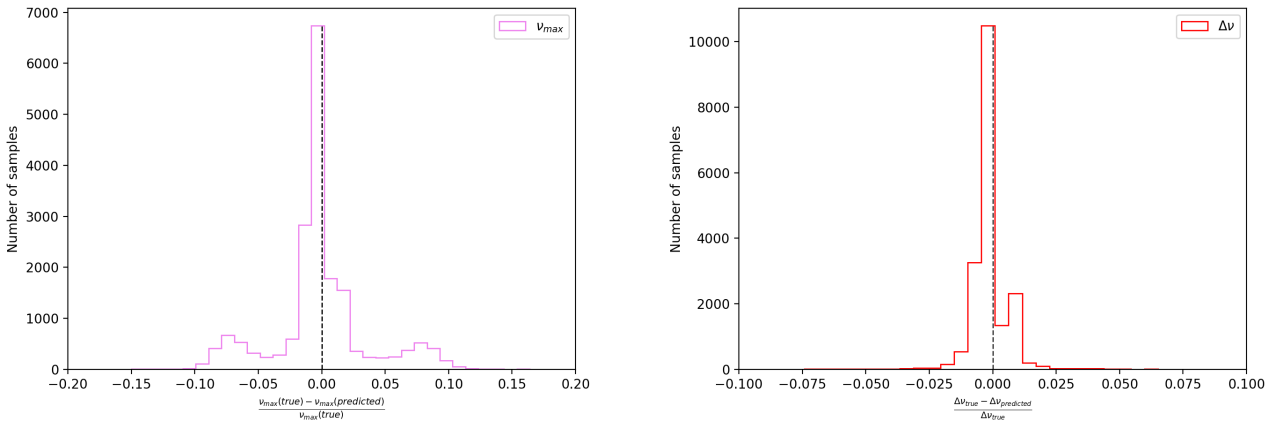

(a) (b)

Figure 13: Histogram of relative errors/fractional residuals for stars in fig 12 **(a)** for ν_{max} and **(b)** for $\Delta\nu$.

Harvey-profile parameters independently of ν_{max}, implying that there is no relation between granulation timescales, amplitudes and relative positions of oscillation signal, unlike in observations and described in section 3.4.1.

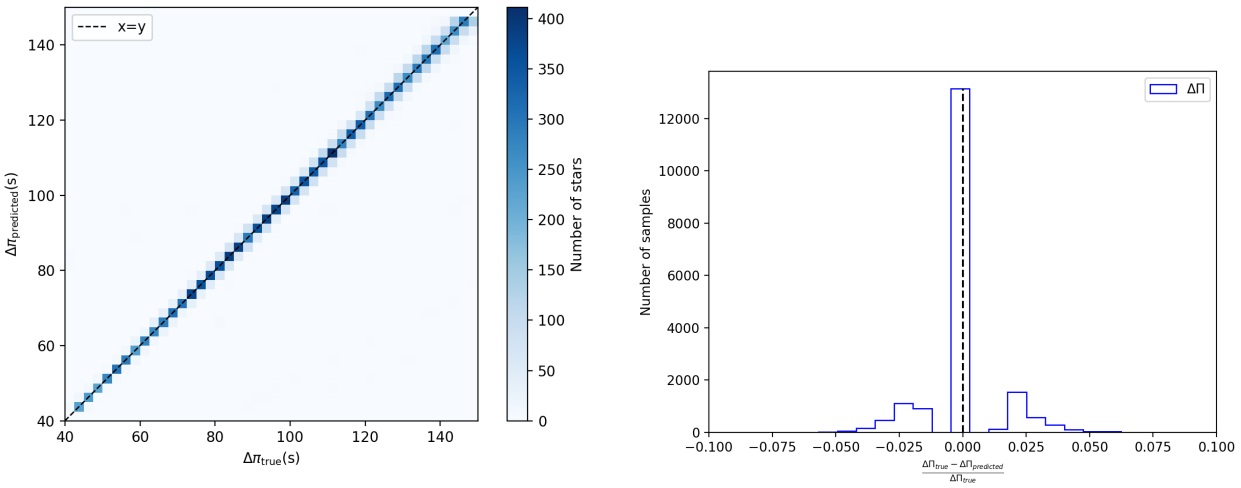

(a) (b)

Figure 14: **(a)** Confusion matrix for $\Delta\Pi_1$ predictions vs true values from the test set of synthetics. **(b)** Histogram of relative errors/fractional residuals for samples in (a).

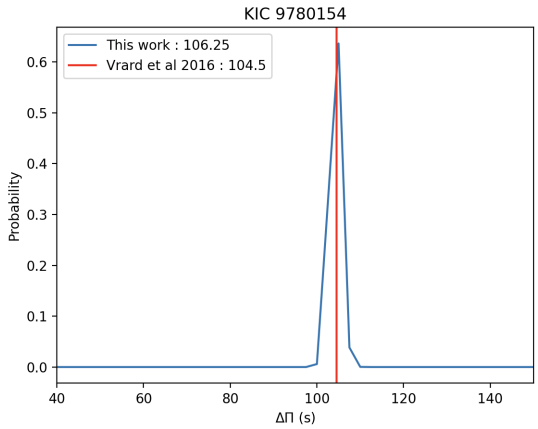

Figure 15: Comparison of $\Delta\Pi_1$ for one matching star with $\Delta\Pi_1 > 100$ μHz in `K2 Model-2` inferences from 3-month Kepler data and corresponding values derived from 4 years of observations by Vrard et al. (2016).

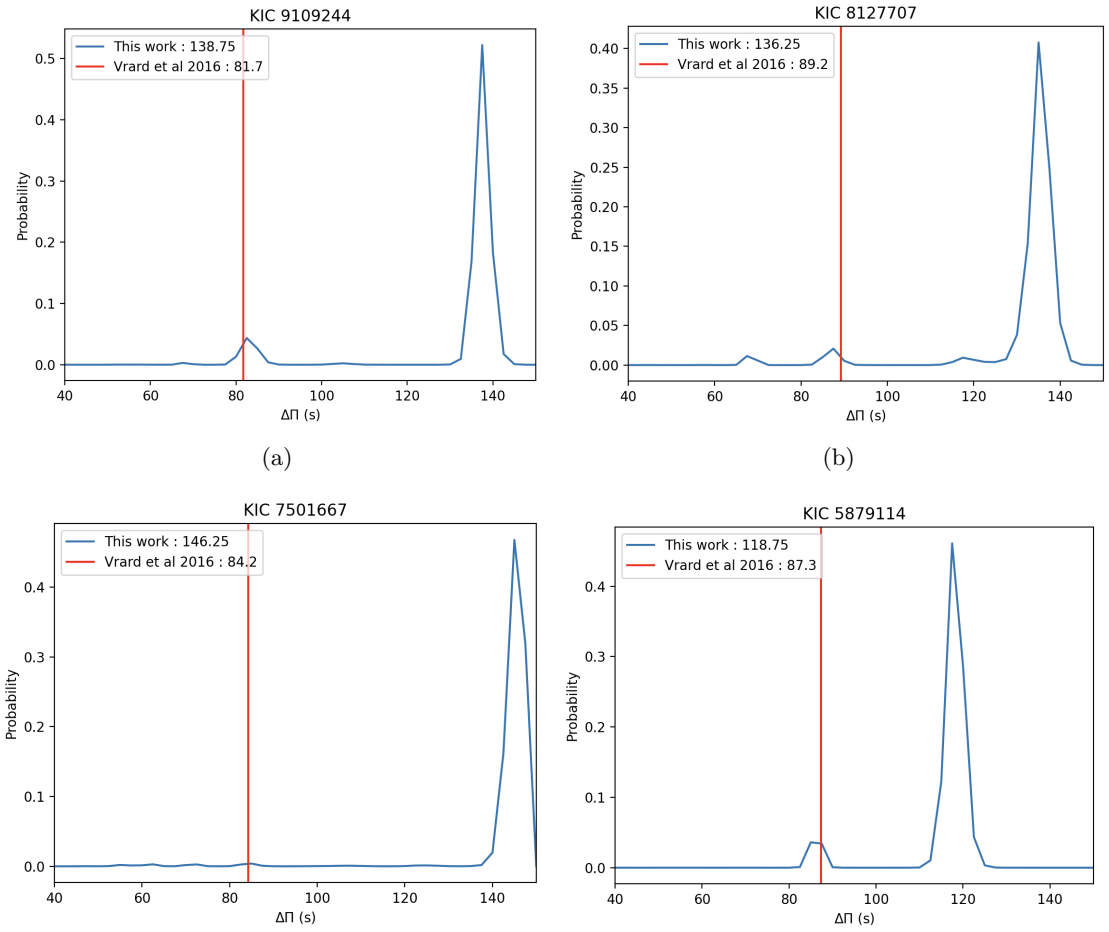

Figure 16: Comparison of $\Delta\Pi_1$ for 4 non-matching stars in `K2 Model-2` inferences from 3-month Kepler data and values derived from 4 years of observations by Vrard et al. (2016) .

Table 3. Inferences for K2 red giants.

index	EPIC	numax (μHz)	dnu (μHz)	dpi (s)	err_dpi (s)	err_dpi_left (s)	err_dpi_right (s)	err_numax (μHz)	err_dnu (μHz)	anomalous
1	201211472	237.0	18.25	91.25	3.72	2.15	1.57	7.5	0.17	0
2	201260990	227.0	16.75	88.75	1.79	0.9	0.9	17.57	0.15	0
3	201420000	187.0	15.15	86.25	2.03	1.02	1.02	16.65	0.14	0
4	201433730	131.0	11.05	81.25	3.29	1.99	1.3	11.42	0.13	0
5	201579693	147.0	12.15	146.25	6.05	3.14	2.91	12.91	0.15	1
6	201583796	179.0	13.65	86.25	3.41	2.0	1.41	7.37	0.15	0
7	201584014	195.0	15.25	86.25	1.95	0.97	0.97	9.52	0.14	0
8	201668891	185.0	14.65	83.75	3.35	1.45	1.91	6.35	0.18	0
9	201696302	193.0	14.65	141.25	4.28	2.14	2.14	14.38	0.17	1
10	201705355	183.0	15.15	86.25	2.17	1.11	1.06	9.67	0.28	0
11	201722103	207.0	15.85	86.25	2.85	1.16	1.69	15.89	0.14	0
12	201722849	219.0	15.95	86.25	3.28	1.99	1.3	18.74	0.16	0
13	201741965	239.0	17.65	91.25	3.58	1.57	2.01	18.15	0.14	0
14	201764418	189.0	15.75	86.25	3.46	1.49	1.97	17.3	0.18	0
15	201779253	169.0	13.75	71.25	2.25	1.12	1.12	5.65	0.14	0
16	201868205	233.0	17.75	91.25	4.31	2.49	1.82	10.2	0.2	0
17	201920393	227.0	16.75	88.75	3.16	1.91	1.25	9.73	0.14	0
18	205994284	163.0	13.65	83.75	2.13	1.06	1.06	12.81	0.14	0
19	206049476	219.0	16.75	88.75	1.79	0.9	0.9	15.01	0.16	0
20	206131981	141.0	12.25	146.25	4.92	2.69	2.23	6.78	0.27	1
21	206136293	203.0	16.05	88.75	2.44	1.37	1.07	16.32	0.15	0
22	206166135	181.0	15.25	86.25	1.75	0.87	0.87	15.89	0.15	0
23	206211295	231.0	17.65	91.25	2.0	1.0	1.0	15.19	0.14	0
24	206476223	167.0	14.05	86.25	2.27	1.22	1.05	7.88	0.15	0
25	206515124	185.0	15.65	88.75	3.09	1.85	1.24	16.2	0.11	0
26	210563947	151.0	12.35	81.25	3.59	1.49	2.11	12.58	0.19	0
27	210653298	179.0	14.45	86.25	3.84	2.17	1.67	14.8	0.2	0
28	210733885	169.0	14.05	86.25	3.44	1.72	1.72	6.46	0.27	0
29	210749402	143.0	12.45	81.25	2.05	1.03	1.03	9.62	0.14	0
30	210791216	191.0	15.25	86.25	2.45	1.06	1.39	11.29	0.15	0
31	210845917	241.0	17.15	88.75	3.45	1.91	1.54	16.97	0.14	0
32	211143318	191.0	14.85	103.75	2.92	1.27	1.65	14.08	0.13	1
33	211307434	149.0	12.35	81.25	3.84	1.61	2.23	5.85	0.17	0
34	211417815	217.0	16.45	88.75	1.92	0.96	0.96	18.32	0.15	0
35	211528211	185.0	14.55	83.75	2.23	1.03	1.2	9.52	0.17	0
36	211540713	183.0	14.05	83.75	3.4	1.51	1.89	14.44	0.15	0
37	211609177	199.0	15.55	86.25	1.9	0.95	0.95	3.77	0.13	0
38	211678470	163.0	13.15	83.75	2.99	1.17	1.82	14.15	0.15	0
39	211704166	183.0	14.35	86.25	1.97	0.99	0.99	11.05	0.14	0
40	211732416	241.0	17.55	88.75	3.35	1.94	1.41	9.1	0.17	0
41	211741853	223.0	17.55	91.25	1.83	0.92	0.92	15.37	0.15	0
42	211781371	169.0	13.25	98.75	4.02	1.84	2.18	7.25	0.14	0
43	211803126	165.0	13.15	81.25	2.6	1.5	1.1	15.12	0.1	0
44	211889864	157.0	13.45	131.25	6.26	3.34	2.93	3.51	0.18	1
45	211897908	197.0	15.35	108.75	4.51	2.49	2.02	10.57	0.15	1

Index	EPIC	numax	dnu	dpi	err_dpi	err_dpi_left	err_dpi_right	err_numax	err_dnu	anomalous
46	211906415	161.0	12.85	88.75	2.78	1.12	1.66	4.34	0.15	0
47	211906830	201.0	14.85	83.75	3.3	1.35	1.95	18.71	0.15	0
48	211929298	175.0	14.45	83.75	2.94	1.15	1.79	12.37	0.21	0
49	211929421	165.0	13.55	86.25	4.0	2.34	1.66	14.79	0.14	0
50	211954121	171.0	14.25	83.75	3.02	1.16	1.86	13.1	0.17	0
51	211974782	213.0	16.35	88.75	3.62	2.15	1.48	10.72	0.13	0
52	211977001	201.0	14.85	83.75	3.64	1.52	2.12	14.7	0.16	0
53	211982071	201.0	15.65	86.25	2.01	1.01	1.01	15.36	0.12	0
54	212010612	187.0	14.85	86.25	1.88	0.94	0.94	8.45	0.14	0
55	212139873	131.0	11.35	78.75	1.99	0.99	0.99	3.38	0.1	0
56	212177247	203.0	16.15	88.75	3.06	1.21	1.85	15.63	0.19	0
57	212207491	197.0	16.35	88.75	2.14	1.06	1.09	7.18	0.19	0
58	212207638	223.0	16.75	88.75	3.25	1.96	1.29	8.27	0.14	0
59	212227531	221.0	16.95	88.75	3.84	1.99	1.85	15.99	0.17	0
60	212297049	215.0	17.05	91.25	3.32	1.98	1.34	7.06	0.14	0
61	212366315	181.0	14.45	83.75	2.64	1.55	1.09	14.38	0.14	0
62	212371042	123.0	11.55	81.25	3.31	1.98	1.33	11.17	0.14	0
63	212610492	195.0	15.35	86.25	2.85	1.18	1.68	5.31	0.34	0
64	212642718	189.0	14.85	83.75	2.93	1.22	1.7	5.28	0.19	0
65	212653037	153.0	12.65	81.25	3.81	2.44	1.37	5.07	0.14	0
66	214776552	163.0	12.85	81.25	3.5	1.29	2.21	14.79	0.17	0
67	220224794	171.0	13.35	81.25	1.99	1.0	1.0	18.39	0.12	0
68	220287156	175.0	13.65	81.25	3.51	1.84	1.66	4.65	0.17	0
69	220327551	203.0	15.35	83.75	2.22	1.08	1.14	12.83	0.16	0
70	220362185	221.0	17.55	88.75	3.44	1.67	1.76	14.8	0.11	0
71	220379656	177.0	14.25	83.75	2.73	1.11	1.62	16.55	0.15	0
72	220391836	151.0	12.85	81.25	3.7	1.28	2.41	14.02	0.16	0
73	220547602	127.0	11.05	81.25	3.58	2.21	1.37	12.74	0.8	0
74	228839832	213.0	16.85	88.75	4.17	2.45	1.72	5.12	0.15	0
75	234469630	149.0	12.55	81.25	2.02	1.01	1.01	16.46	0.13	0
76	246112343	159.0	13.85	83.75	3.66	1.59	2.07	13.45	0.18	0
77	246139560	185.0	14.35	86.25	2.17	1.09	1.09	8.46	0.14	0
78	246233563	215.0	17.25	91.25	1.95	0.97	0.97	15.2	0.11	0
79	246238698	205.0	15.65	88.75	3.43	1.86	1.57	15.86	0.13	0
80	246347334	153.0	13.15	83.75	2.72	1.61	1.12	3.1	0.15	0
81	246416522	229.0	16.35	86.25	3.61	1.82	1.78	13.85	0.16	0
82	246500947	167.0	13.55	71.25	3.55	1.26	2.29	5.44	0.14	0
83	247136733	183.0	14.65	86.25	3.66	2.13	1.53	9.13	0.15	0
84	247141427	217.0	15.85	83.75	3.29	1.34	1.95	17.0	0.15	0
85	247361881	159.0	13.45	83.75	2.37	1.25	1.12	15.29	0.14	0
86	247376509	153.0	12.65	81.25	3.12	1.23	1.9	13.85	0.16	0
87	248599469	181.0	14.85	83.75	2.66	1.11	1.55	15.91	0.16	0
88	248628691	199.0	15.35	86.25	2.06	1.03	1.03	8.97	0.12	0
89	248641221	167.0	13.95	83.75	3.6	1.51	2.09	14.1	0.19	0
90	248657894	155.0	13.45	83.75	3.41	1.54	1.86	3.49	0.19	0
91	248785923	129.0	11.05	78.75	1.84	0.92	0.92	12.3	0.13	0
92	248867024	183.0	14.65	86.25	3.42	1.94	1.48	16.05	0.13	0
93	249379090	177.0	14.65	86.25	3.65	2.18	1.47	5.24	0.12	0

Index	EPIC	numax	dnu	dpi	err_dpi	err_dpi_left	err_dpi_right	err_numax	err_dnu	anomalous
94	249438765	207.0	16.65	86.25	3.96	1.74	2.22	12.93	0.18	0
95	249583241	187.0	14.65	76.25	1.95	0.97	0.97	14.48	0.13	0
96	249586592	187.0	14.55	83.75	4.02	1.85	2.17	14.92	0.25	0
97	249599650	207.0	15.65	88.75	2.58	1.5	1.08	22.04	0.11	0

Note: Machine readable table is provided as supplementary material.

REFERENCES

Abadi, M., Agarwal, A., Barham, P., et al. 2015. https://www.usenix.org/system/files/conference/osdi16/osdi16-abadi.pdf

Aerts, C., Christensen-Dalsgaard, J., & Kurtz, D. W. 2010, Asteroseismology, doi: 10.1007/978-1-4020-5803-5

Anders, F., Chiappini, C., Minchev, I., et al. 2017, A&A, 600, A70, doi: 10.1051/0004-6361/201629363

Baglin, A., Auvergne, M., Boisnard, L., et al. 2006, in 36th COSPAR Scientific Assembly, Vol. 36, 3749

Bedding, T. R., Mosser, B., Huber, D., et al. 2011, Nature, 471, 608, doi: 10.1038/nature09935

Benomar, O. 2023, Power Spectrum Simulator for Solar-like stars, Siddharth2023, Zenodo, doi: 10.5281/zenodo.8296459

Borucki, W. J., Koch, D., Basri, G., et al. 2010, Science, 327, 977, doi: 10.1126/science.1185402

Chaplin, W. J., Kjeldsen, H., Bedding, T. R., et al. 2011, ApJ, 732, 54, doi: 10.1088/0004-637X/732/1/54

Deheuvels, S., Ballot, J., Beck, P. G., et al. 2015, A&A, 580, A96, doi: 10.1051/0004-6361/201526449

Dhanpal, S., Benomar, O., Hanasoge, S., et al. 2022, ApJ, 928, 188, doi: 10.3847/1538-4357/ac5247

—. 2023, ApJ, 958, 63, doi: 10.3847/1538-4357/ad0046

Gaia Collaboration, Brown, A. G. A., Vallenari, A., et al. 2018, A&A, 616, A1, doi: 10.1051/0004-6361/201833051

—. 2021, A&A, 649, A1, doi: 10.1051/0004-6361/202039657

García, R. A., & Ballot, J. 2019, Living Reviews in Solar Physics, 16, 4, doi: 10.1007/s41116-019-0020-1

Gehan, C., Mosser, B., Michel, E., Samadi, R., & Kallinger, T. 2018, A&A, 616, A24, doi: 10.1051/0004-6361/201832822

Goupil, M. J., Mosser, B., Marques, J. P., et al. 2013, A&A, 549, A75, doi: 10.1051/0004-6361/201220266

Grosjean, M., Dupret, M. A., Belkacem, K., et al. 2014, A&A, 572, A11, doi: 10.1051/0004-6361/201423827

Handberg, R., Lund, M. N., White, T. R., et al. 2021, AJ, 162, 170, doi: 10.3847/1538-3881/ac09f1

Harris, C. R., Millman, K. J., van der Walt, S. J., et al. 2020, Nature, 585, 357, doi: 10.1038/s41586-020-2649-2

Hatt, E., Nielsen, M. B., Chaplin, W. J., et al. 2023, A&A, 669, A67, doi: 10.1051/0004-6361/202244579

Hon, M., Kuszlewicz, J. S., Huber, D., Stello, D., & Reyes, C. 2022, AJ, 164, 135, doi: 10.3847/1538-3881/ac8931

Hon, M., Stello, D., García, R. A., et al. 2019, MNRAS, 485, 5616, doi: 10.1093/mnras/stz622

Hon, M., Stello, D., & Zinn, J. C. 2018, ApJ, 859, 64, doi: 10.3847/1538-4357/aabfdb

Hon, M., Huber, D., Kuszlewicz, J. S., et al. 2021, ApJ, 919, 131, doi: 10.3847/1538-4357/ac14b1

Howell, S. B., Sobeck, C., Haas, M., et al. 2014, PASP, 126, 398, doi: 10.1086/676406

Huber, D., Bedding, T. R., Stello, D., et al. 2011, ApJ, 743, 143, doi: 10.1088/0004-637X/743/2/143

Kallinger, T., & Matthews, J. M. 2010, ApJL, 711, L35, doi: 10.1088/2041-8205/711/1/L35

Kamiaka, S., Benomar, O., & Suto, Y. 2018, MNRAS, 479, 391, doi: 10.1093/mnras/sty1358

Kjeldsen, H., & Bedding, T. R. 2011, A&A, 529, L8, doi: 10.1051/0004-6361/201116789

Lightkurve Collaboration, Cardoso, J. V. d. M., Hedges, C., et al. 2018, Lightkurve: Kepler and TESS time series analysis in Python, Astrophysics Source Code Library. http://ascl.net/1812.013

Lomb, N. R. 1976, Ap&SS, 39, 447, doi: 10.1007/BF00648343

Lund, M. N., Miesch, M. S., & Christensen-Dalsgaard, J. 2014, ApJ, 790, 121, doi: 10.1088/0004-637X/790/2/121

Lund, M. N., Handberg, R., Buzasi, D. L., et al. 2021, ApJS, 257, 53, doi: 10.3847/1538-4365/ac214a

Mackereth, J. T., Miglio, A., Elsworth, Y., et al. 2021, MNRAS, 502, 1947, doi: 10.1093/mnras/stab098

Mathur, S., Hekker, S., Trampedach, R., et al. 2011, ApJ, 741, 119, doi: 10.1088/0004-637X/741/2/119

Miglio, A., Chiappini, C., Mackereth, J. T., et al. 2021, A&A, 645, A85, doi: 10.1051/0004-6361/202038307

Montalbán, J., Miglio, A., Noels, A., et al. 2013, ApJ, 766, 118, doi: 10.1088/0004-637X/766/2/118

Mosser, B., Vrard, M., Belkacem, K., Deheuvels, S., & Goupil, M. J. 2015, A&A, 584, A50, doi: 10.1051/0004-6361/201527075

Mosser, B., Barban, C., Montalbán, J., et al. 2011, A&A, 532, A86, doi: 10.1051/0004-6361/201116825

Mosser, B., Goupil, M. J., Belkacem, K., et al. 2012, A&A, 540, A143, doi: 10.1051/0004-6361/201118519

Press, W. H., & Rybicki, G. B. 1989, ApJ, 338, 277, doi: 10.1086/167197

Rauer, H., Aerts, C., Cabrera, J., et al. 2024, arXiv e-prints, arXiv:2406.05447, doi: 10.48550/arXiv.2406.05447

Reback, J., jbrockmendel, McKinney, W., et al. 2022, pandas-dev/pandas: Pandas 1.4.3, v1.4.3, Zenodo, doi: 10.5281/zenodo.6702671

Ricker, G. R., Winn, J. N., Vanderspek, R., et al. 2015, Journal of Astronomical Telescopes, Instruments, and Systems, 1, 014003, doi: 10.1117/1.JATIS.1.1.014003

Scargle, J. D. 1982, ApJ, 263, 835, doi: 10.1086/160554

Sharma, S., Stello, D., Bland-Hawthorn, J., et al. 2019, MNRAS, 490, 5335, doi: 10.1093/mnras/stz2861

Silva Aguirre, V., Bojsen-Hansen, M., Slumstrup, D., et al. 2018, MNRAS, 475, 5487, doi: 10.1093/mnras/sty150

Silva Aguirre, V., Stello, D., Stokholm, A., et al. 2020, ApJL, 889, L34, doi: 10.3847/2041-8213/ab6443

Stello, D., Chaplin, W. J., Basu, S., Elsworth, Y., & Bedding, T. R. 2009, MNRAS, 400, L80, doi: 10.1111/j.1745-3933.2009.00767.x

Stello, D., Saunders, N., Grunblatt, S., et al. 2022, MNRAS, 512, 1677, doi: 10.1093/mnras/stac414

Stewart, L., Bach, F., Berthet, Q., & Vert, J.-P. 2022, arXiv e-prints, arXiv:2211.05641, doi: 10.48550/arXiv.2211.05641

Sullivan, P. W., Winn, J. N., Berta-Thompson, Z. K., et al. 2015, ApJ, 809, 77, doi: 10.1088/0004-637X/809/1/77

Vanderburg, A., & Johnson, J. A. 2014, PASP, 126, 948, doi: 10.1086/678764

Vrard, M., Mosser, B., & Samadi, R. 2016, A&A, 588, A87, doi: 10.1051/0004-6361/201527259

Yu, J., Huber, D., Bedding, T. R., et al. 2018, ApJS, 236, 42, doi: 10.3847/1538-4365/aaaf74

Zhou, J., Bi, S., Yu, J., et al. 2024, The Astrophysical Journal Supplement Series, 271, 17, doi: 10.3847/1538-4365/ad18db

Zinn, J. C., Stello, D., Elsworth, Y., et al. 2022, ApJ, 926, 191, doi: 10.3847/1538-4357/ac2c83